Published in final edited form as:
Brain Struct Funct. 2014 March ; 219(2): 551–569. doi:10.1007/s00429-013-0517-7.

More insights into early brain development through statistical analyses of eigen-structural elements of diffusion tensor imaging using multivariate adaptive regression splines

Yasheng Chen,
Department of Radiology, Biomedical Research Imaging Center, University of North Carolina at Chapel Hill, Chapel Hill, NC 27599, USA

Hongtu Zhu,
Department of Biostatistics, University of North Carolina at Chapel Hill, Chapel Hill, NC 27599, USA

Hongyu An,
Department of Radiology, Biomedical Research Imaging Center, University of North Carolina at Chapel Hill, Chapel Hill, NC 27599, USA

Diane Armao,
Department of Radiology, Biomedical Research Imaging Center, University of North Carolina at Chapel Hill, Chapel Hill, NC 27599, USA; Department of Pathology and Laboratory Medicine, University of North Carolina at Chapel Hill, Chapel Hill, NC 27599, USA

Dinggang Shen,
Department of Radiology, Biomedical Research Imaging Center, University of North Carolina at Chapel Hill, Chapel Hill, NC 27599, USA

John H. Gilmore, and
Department of Psychiatry, University of North Carolina at Chapel Hill, Chapel Hill, NC 27599, USA

Weili Lin
Department of Radiology, Biomedical Research Imaging Center, University of North Carolina at Chapel Hill, Chapel Hill, NC 27599, USA

Abstract

The aim of this study was to characterize the maturational changes of the three eigenvalues ($\lambda_1 \geq \lambda_2 \geq \lambda_3$) of diffusion tensor imaging (DTI) during early postnatal life for more insights into early brain development. In order to overcome the limitations of using presumed growth trajectories for regression analysis, we employed Multivariate Adaptive Regression Splines (MARS) to derive data-driven growth trajectories for the three eigenvalues. We further employed Generalized Estimating Equations (GEE) to carry out statistical inferences on the growth trajectories obtained with MARS. With a total of 71 longitudinal datasets acquired from 29 healthy, full-term pediatric subjects, we found that the growth velocities of the three eigenvalues were highly correlated, but significantly different from each other. This paradox suggested the existence of mechanisms coordinating the maturations of the three eigenvalues even though different physiological origins may be responsible for their temporal evolutions. Furthermore, our results revealed the limitations of using the average of λ_2 and λ_3 as the radial diffusivity in interpreting DTI findings during early

yasheng_chen@med.unc.edu.

brain development because these two eigenvalues had significantly different growth velocities even in central white matter. In addition, based upon the three eigenvalues, we have documented the growth trajectory differences between central and peripheral white matter, between anterior and posterior limbs of internal capsule, and between inferior and superior longitudinal fasciculus. Taken together, we have demonstrated that more insights into early brain maturation can be gained through analyzing eigen-structural elements of DTI.

Keywords

DTI longitudinal analysis; DTI regression analysis; Early brain development; GEE; Multivariate adaptive regression splines

Introduction

Population-based growth statistics derived from pediatric subjects enable us to gain more understandings into the complex process of early brain development with an augmented statistical power. The versatility of diffusion tensor imaging (DTI) (Basser and Pierpaoli 1996; Le Bihan et al. 1986) sheds light on brain maturation through the apparent changes of several water diffusion-related observations such as fractional anisotropy (FA) map, mean diffusivity (MD) map, and white matter tractography. Even though it is well documented that FA increases and MD decreases in early brain development (Neil et al. 1998; Zhai et al. 2003), the maturational changes of individual eigen-structural elements have not been investigated systematically.

FA and MD are composite DTI indices derived from all three eigenvalues of a diffusion tensor matrix ($\lambda_1 \geq \lambda_2 \geq \lambda_3$), and these three eigenvalues represent water diffusivities along the three perpendicular principal directions, respectively (Fig. 1). As demonstrated in Fig. 1, multiple combinations of the three eigenvalues may result in the same FA or MD value. Thus, FA- and MD-based studies were concerned with their less physiological specificity in discerning the different effects on water diffusion brought by changes from white matter axon and myelin sheath. In light of this limitation, a hypothesis assuming λ_1 and $(\lambda_2 + \lambda_3)/2$ as the water diffusivities along (axonal diffusivity, AD) and perpendicular (radial diffusivity, RD) to the white matter tracts emerged. This hypothesis originated from an observation that AD and RD might distinguish axonal injury and myelin dysfunction in animal models (Song et al. 2003). The AD/RD hypothesis has been adopted in interpreting DTI changes associated with early brain myelination process in ROI-based (Gao et al. 2008) and white matter tract-based (Geng et al. 2012) studies. Given the significantly more complex white matter structures in human than in rodent brain, it remains unclear as to what extent is this assumption applicable to human early brain development. In a previous study, we examined the growth trajectories of geometrical diffusion attributes, *C*l $[(\lambda_1 - \lambda_2)/ (\lambda_1 + \lambda_2 + \lambda_3)]$ and *C*p $[2 \times (\lambda_2 - \lambda_3)/(\lambda_1 + \lambda_2 + \lambda_3)]$ and found that *C*p increased significantly in peripheral but not in central white matter. This finding suggested the difference in the growth velocities between the secondary and tertiary eigenvalues in the peripheral white matter, and thus, the applicability of the AD/RD hypothesis may depend upon local white matter structures (Chen et al. 2011). But similar to FA or MD, *C*l and *C*p remain to be composite DTI indices, and multiple combinations of the three eigenvalues can lead to indiscernible temporal changes. *C*l and *C*p reflect the relative ratios between the differences of the eigenvalues and MD, and they cannot directly reveal whether two eigenvalues have similar growth velocities. It is only after determining whether λ_2 and λ_3 have a similar growth velocity that we are able to reveal the applicability of the RD hypothesis in modeling early brain development, which is one objective of this proposed study. To the best of our knowledge, a systematic exploration along this direction remains lacking.

Multiple studies have demonstrated that the white matter maturational process is highly nonlinear throughout different stages of life. In preterm infants, Mckinstry et al. (McKinstry et al. 2002), and Gupta et al. (2005) have observed an initial increase followed by a gradual decrease in FA with a peak at 26–28 weeks of gestational age. In an early postnatal brain study, which overlaps with the age span of this study, Hermoye et al. (2006) reported that the temporal evolution of FA and MD can be represented as a rapid change within the first 12 months, a slow maturation from 12 to 24 months, and a steady state beyond 24 months. It has also been shown that the three eigenvalues follow a nonlinear growth trajectory in selected ROIs (Mukherjee et al. 2001, 2002; Schneider et al. 2004). A nonlinear development was also found in a later developmental stage from 5 to 30 years of age (Lebel et al. 2008). Some recent regression analyses utilized linear fitting with the logarithm of age to model early brain development (Chen et al. 2011; Faria et al. 2010).

This nonlinearity poses great challenges for quantitative studies. Thus far, the choices of the regression model in previous DTI studies were not based upon a thorough interrogation of the data to be analyzed. An empirical choice of a parametric model neglecting the features presented in the data may impose an incorrect prior constraint on the growth trajectory and result in spurious growth patterns with misleading physiological interpretations. In this study, our regression analyses on the eigenvalues will be carried out using a data-driven approach to overcome this major limitation.

It is well documented that myelination progresses from inferior to superior, from posterior to anterior, and from central to peripheral location within brain (Barkovich et al. 1988, 2000). We will utilize the proposed approach to compare posterior (PLIC) to anterior limbs of internal capsule (ALIC) (posterior vs. anterior), inferior (ILF) to superior longitudinal fasciculus (SLF) (inferior vs. superior), and central to peripheral white matter (central vs. peripheral). One previous T1-based study demonstrated that PLIC exhibited high signal intensity at birth, while ALIC did not develop until 2–3 months of age (Barkovich et al. 1988). Previous DTI studies also suggested a late development of SLF (Hermoye et al. 2006; Zhang et al. 2007). The central/peripheral white matter developmental differences have been reported previously in composite DTI indices (Chen et al. 2011; Provenzale 2007; Zhai et al. 2003). Zhai et al. (2003) demonstrated that neonates had higher FA and lower MD in central than in peripheral white matter, and such a difference became smaller in adults. We recently found that geometrical diffusion measures, *C*l and *C*p had different temporal behaviors between central and peripheral white matter. Significant increases in *C*l and *C*p were found in central and peripheral white matter, respectively (Chen et al. 2011).

In this study, we will adopt a Multivariate Adaptive Regression Splines (MARS) method to characterize the nonlinear growth trajectories of the three eigenvalues. MARS can automatically locate the transitional time points (knots) marking the beginnings and endings of the spline segments consisting the whole growth trajectory. The effect of the detected knots on brain growth will be tested using generalized estimating equations (GEE) derived Wald statistics. After adjusting for multiple comparisons through controlling the false discovery rate (FDR), the final regression model will assume the form after removing all the knots contributing insignificantly to the fitting. With this MARS/GEE framework, we will be able to explore the similarities and dissimilarities between growth trajectories of the three eigenvalues from different white matter regions and shed light on whether the secondary and tertiary eigenvalues should be averaged as the radial diffusivity during early brain development.

Materials and methods

Image acquisition and preprocessing

This institutional review board approved study included 29 healthy full-term subjects (17 M and 12 F). Written consents were obtained from each subject's parent before image acquisition. A total of 71 datasets were acquired a few weeks (25 neonates, age 0.07 ± 0.07 years, 14 M and 11 F), 1 year (16 1-year-olds, age 1.05 ± 0.05 years, 9 M and 7 F), 2 years (23 2-year-olds, age 2.03 ± 0.07 years, 14 M and 9 F), and 4 years (7 4-year-olds, age 4.15 ± 0.16 years, 4 M and 3 F) after birth (Fig. 2). At least two longitudinal scans were obtained from each subject in this study. All subjects were fed and calmed to sleep before scanning and ensured to wear ear protections during image acquisition.

Images were acquired with a single-shot double-refocused echo-planar DTI sequence (TR/TE = 5,400/73 ms) with eddy current compensation using a Siemens 3T Allegra head only MR scanner (Siemens, Erlangen, Germany). Diffusion gradients with a *b*-value of 1,000 s/mm^2 were applied in six non-collinear directions with a maximal gradient strength of 40 mT/m and a maximal slew rate of 400 mT/(m msec). An isotropic 2 mm voxel resolution was achieved with contiguous imaging slices covering the whole brain without gap. The in-plane field of view was 256 × 256 mm^2. Multiple acquisitions were averaged to improve the signal-of-noise ratio (SNR) of DTI images. Tensor fitting was performed using the diffusion tensor processing pipelines publicly available from the Oxford University FSL website (http://www.fmrib.ox.ac.uk/fsl/). We followed the pre-processing steps as recommended in (Smith et al. 2007). The FA images obtained from all subjects were co-registered towards a 2-year-old subject (not included in the analysis) using features derived from FA images instead of directly using the FA intensity (Shen 2007).

Multivariate adaptive regression splines (MARS)

In previous DTI analyses on early brain development, a linear fitting with logarithm of age (Eq. 1) was widely used as in (Chen et al. 2011; Faria 2010; Löbel 2009),

$$y_{i,j}=\beta_0+\beta_1\times\log\left(t_{i,j}\right), \quad (1)$$

where $y_{i,j}$ is the *j*th measurement from subject *i*, acquired at age $t_{i,j}$. In addition, another well-utilized model was the 2nd order polynomial regression as demonstrated in Eq. 2,

$$y_{i,j}=\beta_0+\beta_1\times t_{i,j}+\beta_2\times t_{i,j}\times t_{i,j} \quad (2)$$

These two fitting schemes imposed a "shape constraint" on the growth trajectory, and unrealistic growth trajectories would be obtained if this constraint does not agree with the data. On the contrary, MARS was developed as a data-driven approach to approximate complex patterns in regression analysis without imposing any prior constraint on the growth trajectory (Friedman 1993). This statistical method can be considered as a special case for tree-based regression and classification method. Basically, it performed partition of the feature space with a set of linear functions in the format of $(x–t)^+$ and $(t–x)$

$$\begin{aligned}(x-t)^+ &= \begin{cases} x-t, & \text{if } x>t \\ 0, & \text{otherwise}\end{cases} \quad \text{and} \\ (t-x)^+ &= \begin{cases} t-x, & \text{if } t>x \\ 0, & \text{otherwise}\end{cases}\end{aligned} \quad (3)$$

These two functions are reflected pairs and also called hinge functions. The end point, *t* in Eq. 3 is also called a knot, indicating the end of one segment of the growth trajectory and the beginning of another. An unknown function *f(x)* can be approximated as an addictive function with the basis functions obtained from these reflection pairs at a series of knots as in Eq. 4:

$$f(x) = \beta_0 + \sum_{m=1}^{M} \beta_m h_m(x), \quad (4)$$

in which $h_m(x)$ is the basis function formed by the multiplication of several hinge functions, and the coefficients (β_0, β_1,…β_M) can be easily solved by minimizing the least square errors of fitting.

The model building process of MARS consisted of forward and backward steps. The forward step started with fitting the data using a constant β_0 (locating the baseline of the data). At each forward step, among all the possible knots (usually taken as the time points when data were acquired), the one produced the largest decrease in the residual sum of squared error was added to the model. MARS continued to search for all possible knot locations until a maximal number of knots was reached. Usually, a large collection of basis functions were produced after the forward step and the generated model might overfit the data. The backward step pruned the model by removing the basis functions with insignificant contribution to the model. In each pruning step, the term causing the smallest reduction in the residual sum of the squared error was deleted, resulting in a model with a smaller size, and the best model was chosen as the one minimizing the generalized cross-validation criteria as in Eq. 5:

$$GCV(M) = \frac{\sum_{i=1}^{N} [y_i - f_M(xi)]^2}{N[1 - C(M)/N]^2}, \quad (5)$$

where *N* is the total number of data to be fitted, and *C(M)* is the cost complexity measure of a model containing *M* basis functions. The numerator is the sum of squared residuals, and the denominator acts as a penalty for model complexity (Friedman 1993).

GEE method for longitudinal analysis

In this work, the piecewise linear model with the *m* knots (k_1, k_2, …, k_m) identified with MARS was analyzed first,

$$\begin{aligned} E(y_{i,j}) = \quad & \beta_0 + \beta_1 \times t + \beta_2 \times (t - k_1)^+ + \beta_3 \times (t - k_2)^+ \\ & + \ldots + \beta_m (t - k_m)^+. \end{aligned} \quad (6)$$

The coefficients, (β_0, β_1,…β_M) in Eq. 6 were solved as least square solutions assuming a Markov working correlation structure with a weaker correlation between the repeated measurements from the same subject with a longer time separation. The details of the mathematical calculation can be found in (Li et al. 2011; Liang and Zeger1986). The null hypothesis in the format of H_0: $\boldsymbol{R\beta = b_0}$ was tested to determine whether these knots make significant contribution to the growth trajectory. $\boldsymbol{R}$ is an $r \times (m + 2)$ matrix with *r* linear hypotheses to be tested, and b_0 is an $r \times 1$ vector, and *m* is the number of knots. Wald statistic (Eq. 7) was compared against a Chi square distribution for hypothesis testing.

$$X^2=(\boldsymbol{R}\beta-\boldsymbol{b_0})'\left[\boldsymbol{R}\boldsymbol{V}(\beta)\boldsymbol{R}'\right]^{-1}(\boldsymbol{R}\beta-\boldsymbol{b_0}), \quad (7)$$

where $V(\beta)$ is the robust estimation of the covariance of β. If the null hypothesis is rejected at a prefixed significance level, this evaluated term has a significant association with response. FDR was controlled at the level of 0.05 to adjust for multiple comparisons.

Growth trajectories from selected ROIs

Previous findings indicate that white matter myelination follows an order from central to peripheral, from posterior to anterior, and from inferior to superior part of brain (Barkovich et al. 1988; Brody et al. 1987; Paus et al. 2001).

Central white matter such as corpus callosum and posterior limb of internal capsules consisted of long and compact fibers (Provenzale 2007). In contrast, peripheral white matter is more complex and rich in crossings (Wedeen et al. 2012; Wiegell et al. 2000). Representatives for central white matter included genu (GENU in Fig. 3), splenium (SPLE in Fig. 3), and posterior limb of internal capsule (PLIC in Fig. 3), and the peripheral white matter included a fiber crossing region between corpus callosum and corona radiata (CROS in Fig. 3) (Wiegell et al. 2000; Zhang et al. 2006), a white matter region in the anterior corona radiata close to the fiber crossing (CR in Fig. 3), and the superior longitudinal fasciculus (SLF in Fig. 3) (Wiegell et al. 2000; Zhang et al. 2006). ROIs of various sizes were employed to ensure the robustness of the finding. The ROIs were initially chosen as $0.6 \times 0.6 \times 0.6$ cm^3 ($3 \times 3 \times 3$ voxels), $1 \times 1 \times 1$ cm^3 ($5 \times 5 \times 5$ voxels) and $1.4 \times 1.4 \times 1.4$ cm^3 ($7 \times 7 \times 7$ voxels) cubes centered at each of the above-mentioned locations (two ROIs were included in both hemispheres for symmetric structures). A white matter mask from the joint segmentation of the mean MD and FA images from the seven 4-year-olds were then used to exclude those voxels not located within white matter (Chen et al. 2011). The total remaining volume of the ROIs in central and peripheral regions were, respectively, 0.864, 3.568, 8.624 and 1.296, 5.152, 11.200 cm^3. The three eigenvalues and their differences were compared between the central and peripheral white matter with these three sized ROIs (referred as ROI1, ROI2 and ROI3, respectively) for consistent and robust findings.

In projection white matter pathway, the trajectories from the ROIs within ALIC and PLIC were compared (Fig. 3). In association white matter pathway, the comparison was performed using the ROIs in ILF and SLF (Fig. 3). The ROIs in ILF were selected bilaterally according to a previous work in (Hermoye et al. 2006). Likewise, we have also varied ROI sizes for robust and consistent findings (0.432, 1.872, 4.856 cm^3 for PLIC; 0.376, 1.216, 2.800 cm^3 for ALIC; 0.432, 1.704, 3.344 cm^3 for ILF; 0.432, 1.480, 3.216 cm^3 for SLF). These three different sized ROIs were also referred as ROI1, ROI2, and ROI3.

Results

In this section, we will (1) demonstrate the utility of the MARS/GEE framework for selecting the regression model, (2) present the findings on the similarities and dissimilarities of the growths of the three eigenvalues, and (3) compare the growth trajectories of the three eigenvalues between central and peripheral white matter, between ALIC and PLIC, and between ILF and SLF.

Data-driven growth trajectory in early brain development

Growth trajectories for FA and MD from the genu ROI obtained with three fitting schemes (linear logarithm with time, quadratic and the proposed) were given in Figs. 4 and 5, respectively. The linear logarithm fitting rendered a false rapid ascending and descending

trajectories for FA and MD, respectively, during the early stage, leading to an unrealistic estimation of the initial DTI value at birth (intercept). For instance, the estimated genu FA at birth was lower (Fig. 4B) and the estimated genu MD was higher (Fig. 5B) than peripheral white matter, which contradicted previous findings that central white matter had higher FA and lower MD at birth (Zhai et al. 2003). For quadratic fitting, a peak (or valley) followed by a descending (or ascending) trend was observed for the growth trajectory of FA (or MD). It is apparent that both linear logarithm of time and quadratic fittings resulted in spurious growth trajectories. In contrast, our data-driven approach generated a more realistic growth trajectory with better predictions at both ends, highlighting the necessity for this MARS/GEE framework in modeling DTI changes in early brain development.

Similar knot distributions in the three eigenvalues

As discussed previously, the knots obtained with MARS marked the ending of one segment and the beginning of another along the growth trajectory. The transition of the growth signaled by these knots may potentially correspond to the onset of certain physiological events shaping brain maturation, and such timing information of white matter maturation may be imbedded in the distribution of these knots. The histograms of the knots identified for the three eigenvalues were given in Fig. 6. We found that with the given data, the three eigenvalues had almost identical histograms in the knots identified using MARS (corr(λ_1, λ_2) = 0.994, $p < 10^{-6}$; corr(λ_1, λ_3) = 0.989, $p < 10^{-6}$; and corr(λ_2, λ_3) = 0.997, $p < 10^{-6}$) and these knots heavily distributed around the year marks. Data with a dense temporal sampling are needed to discern whether this finding indeed reflects underlying physiology or arises from the experimental design (the sampling scheme).

Highly correlated growth velocities of the three eigenvalues

As in Fig. 6, the distribution of the knots of the three eigenvalues formed three clusters with medians at 24 days (0.066 years), 377 days (1.033 years), and 739 days (2.025 years), respectively. The initial model for the growth trajectory was formed with the piecewise linear segments transitioned at the medians of these three clusters (Eq. 8).

$$y = \beta_0 + \beta_1 \times t + \beta_2 \times (t - 0.066)^+ + \beta_3 \times (t - 1.033)^+ + \beta_4 \times (t - 2.025)^+ \quad (8)$$

Through the testing procedures outlined previously, the knots located at 0.066 and 2.025 years were removed from the growth trajectories of all the three eigenvalues due to their insignificant contributions to the fitting after adjusting for multiple comparisons. The final selected model for further regression analysis was given as

$$y = \beta_0 + \beta_1 \times t + \beta_2 \times (t - 1.033)^+. \quad (9)$$

As a result, it was justified to approximate the nonlinear growth trajectories of the three eigenvalues with two linear segments (stage **PI** and **PII**) with a transition around 1 year after birth. β_0 (in a unit of 10^{-3} mm^2/s) is the intercept, an estimate of an eigenvalue at birth, β_1 [in a unit of 10^{-3} mm^2/(s × year)] is the growth velocity in stage **PI**, and β_2 (with the same unit as β_1) is the transition in velocity from **PI** to **PII** (the growth velocity is $\beta_1 + \beta_2$ in **PII**). The intercepts and growth velocities in the two stages were given in Figs. 7, 8, 9. It was apparent that in all three eigenvalues, the most rapid reduction occurs within **PI**.

The growth velocities of the three eigenvalues within white matter were highly correlated with each other (**PI**: corr(λ_1, λ_2) = 0.748, $p < 10^{-10}$; corr(λ_1, λ_3) = 0.742, $p < 10^{-10}$; and

corr(λ_2, λ_3) = 0.942, $p < 10^{-10}$; **PII**: corr(λ_1, λ_2) = 0.666, $p < 10^{-10}$; corr(λ_1, λ_3) = 0662, $p < 10^{-10}$; and corr(λ_2, λ_3) = 0.885, $p < 10^{-10}$). After we subtracted the velocity of MD from the three eigenvalues, we found that the λ_1 and λ_2 or λ_3 remained highly correlated in both **PI** (corr(λ_1-MD, λ_2-MD) = −0.789, $p < 10^{-10}$; corr(λ_1-MD, λ_3-MD) = −0.815, $p < 10^{-10}$) and **PII** (corr(λ_1-MD, λ_2-MD) = −0.728, $p < 10^{-10}$; corr(λ_1-MD, λ_3-MD) = −0.713, $p < 10^{-10}$), while the correlation between λ_2 and λ_3 became weaker (**PI**: corr(λ_2-MD, λ_3-MD) = 0.309, $p < 10^{-10}$; **PII**: corr(λ_2-MD, λ_3-MD) = 0.124, $p < 10^{-10}$). Thus, the high correlation between the growth velocities of λ_2 and λ_3 may be attributable to an overall diffusion reduction process indicated through decrease in MD, after removal of which, λ_2 and λ_3 are less correlated with each other.

Differences between the three eigenvalues in both central and peripheral white matter

The estimated β_0, the growth velocities during **PI** and **PII** obtained with the three different sized ROIs (ROI1–ROI3) are given in Table 1 for central and peripheral white matter. The growth trajectories are given in Figs. 10 and 11 for central and peripheral white matter, respectively. In all three ROIs and in both central and peripheral white matter, three eigenvalues demonstrated an initial rapid reduction during **PI** followed by a slower reduction during **PII**.

In both central and peripheral white matter, with paired *t*-tests and after adjusting for multiple comparisons through controlling FDR, growth velocities between λ_1 and λ_2 or λ_3 were significantly different in both **PI** and **PII** ($p < 10^{-6}$ for ROI1–ROI3), while the growth velocities of λ_2 and λ_3 were significantly different from each other only during **PI** ($p < 10^{-6}$ for ROI1–ROI3).

To further confirm the significant differences among the growth velocities of the three eigenvalues, we applied the proposed analysis to λ_1–λ_2 (D_1) and λ_2–λ_3 (D_2, which is a within-plane rotational invariant for the assumed cylindrical structure of diffusion profile in major white matter). For D_1, in central, significant increase was found in **PI** ($p \sim 3.020 \times 10^{-8}$ for ROI1, $p \sim 1.259 \times 10^{-9}$ for ROI2, $p \sim 4.467 \times 10^{-11}$ for ROI3), but **PII** only demonstrated such a trend ($p \sim 0.062$ for ROI1, $p \sim 0.006$ for ROI2, $p \sim 0.005$ for ROI3). In peripheral, D_1 increased significantly both in **PI** ($p \sim 0.002$ for ROI1, $p \sim 2.548 \times 10^{-5}$ for ROI2, $p \sim 2.7542 \times 10^{-8}$ for ROI3) and **PII** ($p \sim 0.0209$ for ROI1, $p \sim 0.0039$ for ROI2, $p \sim 0.0048$ for ROI3). For D_2, consistently significant temporal change was found only during **PI** for both central ($p \sim 6.166 \times 10^{-6}$ for ROI1, $p \sim 4.68 \times 10^{-5}$ for ROI2, $p \sim 2.754 \times 10^{-4}$ for ROI3) and peripheral ($p \sim 2.399 \times 10^{-6}$ for ROI1, $p \sim 1.479 \times 10^{-6}$ for ROI2, $p \sim 2.884 \times 10^{-6}$ for ROI3) white matter. In summary, we have demonstrated consistently significant differences between the growth velocities of the three eigenvalues independent of ROI sizes, suggesting the robustness of these findings.

Central and peripheral white matter differences revealed by regression analysis

The growth trajectories of the three eigenvalues and their differences in central and peripheral white matter were given in Figs. 10 and 11, and statistical comparisons between central and peripheral white matter were summarized in Table 1. Compared with peripheral white matter, the central had a significantly higher λ_1 ($p < 10^{-6}$ for ROI1–ROI3), lower λ_2 ($p < 10^{-6}$ for ROI1–ROI3), lower λ_3 ($p < 10^{-6}$ for ROI1–ROI3), higher D_1 ($p < 10^{-6}$ for ROI1–ROI3), and lower D_2 ($p < 10^{-6}$ for ROI1–ROI3) at birth.

During **PI**, the decreasing velocities were smaller in central than in peripheral white matter in λ_1 ($p < 10^{-6}$ for ROI1–ROI3), λ_2 ($p \sim 0.023051$ for ROI1, $p < 10^{-6}$ for ROI2, $p < 10^{-6}$ for ROI3), and λ_3 ($p \sim 10^{-6}$ for ROI1–ROI3). During **PII**, λ_1 remained decreasing less rapidly in central than in peripheral white matter ($p \sim 0.154$ for ROI1, $p \sim 2 \times 10^6$ for ROI2, $p \sim$

10^{-6} for ROI3), while λ_2 and λ_3 decreased more rapidly in central than in peripheral (λ_2: $p \sim 0.007$ for ROI1, $p \sim 0.008$ for ROI2, $p \sim 0.687$ for ROI3; λ_3: $p \sim 0.004$ for ROI1, $p \sim 0.002$ for ROI2, $p \sim 0.052$ for ROI3).

In **PI**, D_1 increased more rapidly in central than in peripheral white matter ($p < 10^{-6}$ for ROI1–ROI3). The growth velocities of D_2 were opposite in directions between central and peripheral white matter (decreasing in central while increasing in peripheral, $p < 10^{-6}$ for ROI1–ROI3).

During **PII**, the increase in D_1 remained consistently more rapid in central than in peripheral white matter ($p \sim 10^{-6}$ for ROI1–ROI3), while the growth velocity of D_2 was similar between central and peripheral white matter. As shown in Figs. 10 and 11, in both central and peripheral white matter, the temporal increase in D_1 was apparent during both **PI** and **PII**, while the temporal increase in D_2 was only apparent during **PI**. Interestingly, the separation between the growth trajectories of D1 and D2 became increasingly widened in central than peripheral white matter regions.

Inhomogeneity within projection white matter pathway: difference between ALIC and PLIC

The growth trajectories of the three eigenvalues and their differences in ALIC and PLIC were given in Figs. 12 and 13, and the statistical comparisons between ALIC and PLIC were summarized in Table 2. At birth, PLIC had a significantly lower λ_2 ($p < 10^{-6}$ for ROI1–ROI3), λ_3 ($p < 10^{-6}$ for ROI1–ROI3), higher D_1 ($p < 10^{-6}$ for ROI1–ROI3), and higher D_2 ($p < 10^{-6}$ for ROI1–ROI3) than ALIC.

During **PI**, comparing with ALIC, PLIC decreased slower in all three eigenvalues ($p < 10^{-6}$ for ROI1–ROI3), while the comparisons of D_1 and D_2 were not consistent through ROIs (only significantly different in ROI3).

During **PII**, λ_1 remained decreasing slower in PLIC than ALIC ($p < 10^{-6}$ for ROI1–ROI3). The comparisons of the growth velocities of λ_2 were not consistent through ROIs ($p = 0.429$ for ROI1, $p = 0.093$ for ROI2, $p < 10^{-5}$ for ROI3) and the velocities within ALIC and PLIC were comparable in all three ROIs. λ_3 decreased more rapidly in ALIC than in PLIC ($p = 0.004$ for ROI1, $p < 10^{-6}$ for ROI2 and ROI3). D_1 continued to increase in PLIC while remaining almost steady in ALIC ($p < 10^{-6}$ for ROI1–ROI3). Contrary to D_1, the growth velocities in D_2 demonstrated opposite trends in PLIC and ALIC (slight decrease in PLIC while increase in ALIC; $p < 10^{-3}$ for ROI1; $p < 10^{-6}$ for ROI2; $p < 10^{-5}$ for ROI3).

Inhomogeneity in association white matter pathway: difference between ILF and SLF

The growth trajectories of the three eigenvalues and their differences in ILF and SLF are given in Figs. 14 and 15, and the statistical comparisons between ILF and SLF aresummarized in Table 3. Comparing with SLF, ILF had significantly higher values in all three eigenvalues and their differences (λ_1–λ_3: $p < 10^{-6}$ for all ROIs; D1: $p < 10^{-6}$ for all ROIs; D2: $p < 10^{-3}$ for ROI1; $p < 10^{-4}$ for ROI2; $p < 10^{-6}$ for ROI3) at birth.

During **PI**, all three eigenvalues decreased more rapidly in ILF than in SLF (λ_1: $p < 10^{-4}$ for ROI1, $p < 10^{-6}$ for ROI2, $p < 10^{-6}$ for ROI3; λ_2: $p < 10^{-6}$ for all ROIs; λ_3: $p = 0.006$ for ROI1; $p < 10^{-3}$ for ROI2; $p < 10^{-6}$ for ROI3). Comparisons of the growth velocities of D_1 were not consistent across ROIs (ILF [SLF, $p = 0.019$ for ROI1; ILF < SLF, $p = 0.0359$ for ROI2; ILF < SLF, $p = 0.307$ for ROI3). The growth velocities of D_2 were significantly different between ILF and SLF ($p < 10^{-6}$ for all ROIs) and demonstrated opposite trends (decreasing for ILF while increasing for SLF).

During **PII**, similar to **PI**, λ_1 and λ_3 continued to decrease more rapidly in ILF than in SLF (λ_1: $p < 10^{-5}$ for ROI1, $p < 10^{-5}$ for ROI2, $p < 10^{-2}$ for ROI3; λ_2: $p < 0.001$ for ROI1; $p < 10^{-4}$ for ROI2; $p < 0.001$ for ROI3), while λ_2 only demonstrated such a trend ($p < 10^{-4}$ for ROI1, $p = 0.003$ for ROI2, $p = 0.443$ for ROI3). The growth velocities were comparable in D_1 ($p = 0.872$ for ROI1; $p = 0.704$ for ROI2; $p = 0.341$ for ROI3) and D2 remained steady in both ILF and SLF.

Discussion

Advantages of data-driven regression analysis

An appropriate regression analysis is the first necessary step towards a physiologically meaningful inference on the DTI findings in early brain development. For the first time, we introduced MARS to modeling early brain development with DTI regression analysis. In general, the identified nonlinear growth trajectories of the three eigenvalues are consistent with previous DTI studies in early brain development. The automatically detected initially rapid change within the first year followed by a slower maturation afterwards agreed well with the observations by Hermoye et al. (2006). More importantly, our approach achieved a better fitting performance and meaningful physiological inference. The inherently enforced "velocity-acceleration" assumption by quadratic fitting on brain growth was apparently problematic due to the spurious peak (or valley) and the reversed growth trend at the end of trajectory. For the linear regression with the logarithm of time, besides the spuriously rapid ascending/descending trajectories observed close to birth, it is also difficult to make physiological inference on the velocity (β_1 in Eq. 1). In contrast, our data-driven approach does not impose a subjective assumption in the interpretation of the regression results and attributes the nonlinearity of the growth trajectory to changes in velocity. In addition, the knots identified with MARS may carry specific physiological meanings indicating the discontinuities in growth velocity caused by the onsets of certain biological processes. For instance, Provenzale et al. (2007) reported that the brain growth in the first year can be divided into two linear segments with the transition around 100 days, which may be caused by the onset of myelination. To the best of our knowledge, our proposed study is the first one to automatically detect discontinuities in DTI evolution. The proposed method can be adopted to analyze any non-linear changes in brain developments or disease progressions. Interestingly, with the given data, we found an almost identical distribution of knots in the three eigenvalues even though they represent water diffusivities along three orthogonal directions. But this finding may depend on the temporal sampling of the growth curve around year marks in our data. Future studies using data with finer temporal sampling are required to determine whether a common timing mechanism exists in the progression of water diffusion along different directions. If given the densely enough temporal coverage as in (Provenzale 2007), we expect our work to be able to detect the discontinuity around 100 days, which has a steeper slope in velocity transition than the one reported in this study at year 1.

Utilities of our method in modeling white matter development

Brain growth proceeds in a highly ordered and dynamic fashion. Formations of brain gyration were usually before term and proceeded myelination deposition in most white matter regions (Larroche 1977). During normal white matter maturation, axonal development precedes myelination. Within parietal white matter, GAP-43 staining demonstrated a high level of expression in 21–64 post-conceptual weeks and reached adult-like level in 17 post-natal months, while myelin basic protein expression indicated myelination starting around 54 postnatal weeks and progressed to adult-like staining in 72–92 postnatal weeks (Haynes et al. 2005). A more detailed autopsy study revealed that different sites within white matter began myelination at different times and progressed to

maturation over different time intervals. Interestingly, early onset of myelination may not always be followed by early myelin maturation (Kinney et al. 1988). The proposed MARS/GEE based framework is especially suited for exploring the ordered growth in brain, because MARS is able to model both the onset time and the different growth velocities during different developmental stages.

Another potential powerful application of this MARS/GEE framework is to identify the delay in white matter maturation through DTI. White matter myelination was highly correlated with the functional maturation of brain and delayed myelination was found to correlate to the decreased neuro developmental performance (Paus et al. 2001). Children with a developmental delay had a wide-spread increase in MD and decrease in diffusion anisotropy in white matter (Filippi et al. 2003). With our approach, the identified knot sequences between control and patient populations can be used to quantify the delay time in patients. Furthermore, growth velocities at different developmental stages can be compared across groups to delineate abnormality in myelination velocity.

Highly correlated but significantly different growth velocities of the eigenvalues

One interesting finding of this study is that the growth velocities of the three eigenvalues were highly correlated during both **PI** and **PII**, which suggests a concordance among the maturations of the three eigenvalues. The overall diffusion reduction represented by the reduction in MD may lead to the high correlation between λ_2 and λ_3 in both **PI** and **PII**, and the removal of which resulted in much weaker correlations between them. Conversely, after removal of MD, the correlations between λ_1 and λ_2 or λ_3 became slightly stronger in both **PI** and **PII**. Thus, the high correlation between λ1 and λ2 or λ3 was independent of the overall diffusion reduction. In summary, the overall diffusivity reduction represented by reduction in MD may result in the concordance between λ_2 and λ_3, while another mechanism may contribute to the high coordination between the growth velocities of λ_1 and λ_2 or λ_3.

We have also found the growth velocities of the three eigenvalues were significantly different from each other in both central and peripheral white matter, and the significantly different growth trajectories of λ_2 and λ_3 implicated the limitations of the RD hypothesis in modeling early brain development as adopted in (Gao et al. 2008; Geng et al. 2012). Genu, splenium, and posterior limb of internal capsule are the regions most likely consisting of long cylindrical white matter structures with a high likelihood for the application of AD/RD hypothesis. Based on the AD/RD hypothesis, D_2 should be a trivial rotational invariant within the plane perpendicular to the white matter axon in these cylinder-like central white matter tracts. However, significant differences between the growth velocities of λ_2 and λ_3 in central white matter during **PI** (further confirmed by the significant temporal reduction in D_2) demonstrated that the water diffusion within the radial plane became homogeneous gradually during the first year. Taken together, these results suggested that different physiological mechanisms may contribute to the changes of the three eigenvalues at least during the first postnatal year, which cannot be explained by the AD/RD hypothesis.

Central/peripheral white matter differences in maturation

At birth, the significantly higher λ_1 and lower λ_2 and λ_3 in central than in peripheral white matter agrees with the previous finding that central white matter has higher FA values than peripheral regions at birth (Provenzale 2007; Zhai et al. 2003) and this finding is also in line with the more compact nature of the central white matter (Provenzale 2007). The significantly lower D_2 in central than in peripheral white matter also agrees with the more cylinder-like structure in central than in peripheral white matter as reported in our previous study based upon *C*p (Chen et al. 2011). During **PI**, the central white matter had a lower velocity in λ_1 reduction than peripheral, which may indicate the axons are more mature in

central than in peripheral white matter. The difference in growth velocities of λ_2 and λ_3 were more complex. During **PI**, the peripheral white matter had significantly higher reduction in λ_2 and λ_3 than central white matter, suggesting that λ_2 and λ_3 may have different physiological underpinnings between central and peripheral white matter, especially given the more complex fiber structures in peripheral white matter. It is well known that the white matter myelination occurs depending on a *g*-ratio, and white matter myelination started earlier in central white matter such as corpus callosum and posterior limb of internal capsules (Sherman and Brophy 2005). Thus, if AD/RD hypothesis holds, it is expected that the decreasing of λ_2 and λ_3 are more rapid within central than peripheral white matter, which contradicts our observation. Given the complex peripheral white matter structures rich in crossing fiber groups, it is natural to speculate that the temporal changes in λ_2 and λ_3 may also reflect the changes in diffusivity along the fiber axons in these different fiber groups. Interestingly, in contrast to **PI**, λ_2 and λ_3 decreased more rapidly in central than in peripheral white matter during **PII**, but with similar velocities (~–0.04X). Thus, the velocities of λ_2 and λ_3 may be more related to myelination process in **PII** than **PI**.

When we examined the growth trajectories of D_2, this difference decreased in central but increased in peripheral white matter (Figs. 10 and 11), and this clear distinction indicated that different factors, depending on the geometrical locations, may shape their temporal evolutions. In central white matter, the reduction of D_2 may reflect that the water diffusion within the radial plane becomes increasingly more homogeneous during development. But in peripheral white matter, with the recently emerged evidence that crossing white matter tracts assumes a local perpendicular curvilinear structure (Wedeen et al. 2012), the reduced water diffusivity along radial direction may be affected by both myelination and axonal development in several perpendicular fiber groups.

Growth inhomogeneity in projection and association fiber pathways

It is well documented that myelination progresses from an inferior to superior and from a posterior to anterior location (Barkovich 2000; Barkovich et al. 1988). Accordingly, myelination in PLIC and ILF occur earlier than in ALIC and SLF, respectively, even though they belong to the same white matter pathways. Given the previous MR based findings as in (Barkovich et al. 1988; Hermoye et al. 2006; Zhang et al. 2007), we are able to search for DTI features in modeling white matter maturation.

At birth, PLIC had a significantly lower λ_2 and λ_3 compared with ALIC and this finding agreed with previous reports that PLIC had myelin deposition at birth, but not ALIC (Kinney et al. 1988). In **PI**, all three eigenvalues decreased slower in PLIC than ALIC, which may be attributed to the earlier maturation of PLIC. In contrast, even though ILF developed earlier than SLF, ILF had significantly higher values in all three eigenvalues than SLF at birth. In **PI**, all three eigenvalues decreased more rapidly in ILF than SLF and the same trend continued in **PII**. We speculate that slower changes in DTI eigenvalues can only be considered as an indicator of earlier myelination in central but not in peripheral white matter tracts, where complex structures complicate temporal evolutions of different eigenvalues. In contrast, we found that the difference between the growth trajectories of D1 and D2 may be more consistent in reflecting difference in myelination progression. For instance, the difference between the growth trajectories of D_1 and D_2 was apparently greater in PLIC than ALIC (Figs. 12 and 13). The same observation also held true in the comparison between ILF and SLF (Figs. 14 and 15). In ILF the separation between the growth trajectories of D_1 and D_2 became widened with time, while their trajectories intertwined in SLF. We have also observed this same feature presented in the comparison between central and peripheral white matter. Thus, the difference between the growth trajectories of D1 and D2 seemingly agrees with the previously documented order of white matter maturation.

Limitations

Sparse temporal coverage especially within the first postnatal year is one major limitation of our study. As a result, the piecewise linear growth trajectory obtained by MARS should not be considered as an accurate representation of the growth during this period. Instead, the presented results are estimates of the end-to-end growth velocities. Even though we have shown that the growth trajectories of the three eigenvalues were divided into two phases with a transition around 1 year, the clustered temporal sampling forbids us to make further physiological inference upon this transition. In terms of the capability of modeling nonlinearity, the quadratic or linear logarithm models may have the advantage if their inherent assumption is a reasonable approximation to the ground truth.

Second, as a DTI single modality based early brain developmental study, we cannot discern the DTI changes in early brain development caused by myelination and other numerous non-myelin related factors such as axonal diameter change, axon membrane composition change, concentration of microtubules and microfilaments, the activity of Na^+/K^+ pump, and reduction in extracellular space (Prayer et al. 2001). But the timing information obtained with MARS provides us a new means to establish the link between DTI and histological studies. We may be able to disentangle the DTI changes brought by some of these physiological factors if they affect water diffusivities along different directions differently or their onsets are separated in time.

Last, the presented results may be subject to the confound brought by different partial volume effects using the same voxel size across the age span. Newborns have a significantly smaller intracranial volume compared with old children [neonates: 547.43 ± 91.99, 1-year-olds: 1,096.92 ± 100.30, 2-year-olds: 1,193.48 ± 131.03, 4-year-olds: 1,314.93 ± 118.72(cm^3)]. High-resolution DTI pulse sequence producing a smaller voxel size in neonates can overcome this caveat, but with a hefty cost in SNR and imaging time. When reducing the voxel length by half (eight times reduction in volume), SNR becomes eight times lower. To maintain the same SNR, total scan time has to be lengthened 64 times, which is impractical and makes image acquisition prone to motion artifacts. In this study, we have evaluated this confound with an alternative down-sampling approach in images obtained from older children according to the brain volume ratio with respect to neonates. For instance, in 2-year-olds, the average brain volume was 1,193/547 ~ 2.18 times of the average in neonates, and we increased voxel length in 2-year-olds by 1.30 times (~$2.18^{0.333}$) through down-sampling diffusion weighted images, with which we recomputed the three eigenvalues. After co-registering the down-sampled eigenvalue maps towards their original counterparts, we have found high correlations between them within whole brain (correlation coefficients: 0.990 ± 0.002 for λ_1, 0.987 ± 0.002 for λ_2, 0.986 ± 0.002 for λ_3), which partially validates our findings under different partial volume effects across different age groups.

Conclusion

In this study, with the MARS/GEE combined framework, we found that the growth velocities of the three eigenvalues were highly correlated, which may attribute to the mechanisms orchestrating brain development. Moreover, the growth velocities of the three eigenvalues were significantly different between central and peripheral, between anterior and posterior, and between inferior and superior white matter, suggesting our approach is able to model the progressive white matter maturation in space. Furthermore, our results demonstrated the limitations of the AD/RD hypothesis in interpreting DTI findings during early brain development. In conclusion, more insights into early brain development were gained through analyzing the eigen-structural elements of DTI.

Acknowledgments

4 and NIH Grants RR025747-01, P01CA142538-01, MH086633, and AG033387, NIH Grants 1R01EB006733, R01EB008374, and 1R01EB009634, NIH Grants R01MH070890 and R01HD053000, and NIH Grant R01NS055754.

References

Barkovich AJ. Concepts of myelin and myelination in neuroradiology. AJNR Am J Neuroradiol. 2000; 21:1099–1109. [PubMed: 10871022]

Barkovich AJ, Kjos BO, Jackson DE Jr, Norman D. Normal maturation of the neonatal and infant brain: MR imaging at 1.5 T. Radiology. 1988; 166:173–180. [PubMed: 3336675]

Basser PJ, Pierpaoli C. Microstructural and physiological features of tissues elucidated by quantitative-diffusion-tensor MRI. J Magn Reson B. 1996; 111:209–219. [PubMed: 8661285]

Brody BA, Kinney HC, Kloman AS, Gilles FH. Sequence of central nervous system myelination in human infancy. I. An autopsy study of myelination. J Neuropathol Exp Neurol. 1987; 46:283–301. [PubMed: 3559630]

Chen Y, An H, Zhu H, Jewells V, Armao D, Shen D, Gilmore JH, Lin W. Longitudinal regression analysis of spatial-temporal growth patterns of geometrical diffusion measures in early postnatal brain development with diffusion tensor imaging. Neuroimage. 2011; 58:993–1005. [PubMed: 21784163]

Faria AV, Zhang J, Oishi K, Li X, Jiang H, Akhter K, Hermoye L, Lee SK, Hoon A, Stashinko E, Miller MI, van Zijl PC, Mori S. Atlas-based analysis of neurodevelopment from infancy to adulthood using diffusion tensor imaging and applications for automated abnormality detection. Neuroimage. 2010; 52:415–428. [PubMed: 20420929]

Filippi CG, Lin DD, Tsiouris AJ, Watts R, Packard AM, Heier LA, Ulug AM. Diffusion-tensor MR imaging in children with developmental delay: preliminary findings. Radiology. 2003; 229:44–50. [PubMed: 12920176]

Friedman JH. Multivariate adaptive regression splines. Ann Stat. 1993; 19:1–67.

Gao W, Lin W, Chen Y, Gerig G, Smith JK, Jewells V, Gilmore JH. Temporal and spatial development of axonal maturation and myelination of white matter in the developing brain. AJNR Am J Neuroradiol. 2008; 30(2):290–296. [PubMed: 19001533]

Geng X, Gouttard S, Sharma A, Gu H, Styner M, Lin W, Gerig G, Gilmore JH. Quantitative tract-based white matter development from birth to age 2 years. Neuroimage. 2012; 61(3):542–557. [PubMed: 22510254]

Gupta RK, Hasan KM, Trivedi R, Pradhan M, Das V, Parikh NA, Narayana PA. Diffusion tensor imaging of the developing human cerebrum. J Neurosci Res. 2005; 81:172–178. [PubMed: 15931676]

Haynes RL, Borenstein NS, Desilva TM, Folkerth RD, Liu LG, Volpe JJ, Kinney HC. Axonal development in the cerebral white matter of the human fetus and infant. J Comp Neurol. 2005; 484:156–167. [PubMed: 15736232]

Hermoye L, Saint-Martin C, Cosnard G, Lee SK, Kim J, Nassogne MC, Menten R, Clapuyt P, Donohue PK, Hua K, Wakana S, Jiang H, van Zijl PC, Mori S. Pediatric diffusion tensor imaging: normal database and observation of the white matter maturation in early childhood. Neuroimage. 2006; 29:493–504. [PubMed: 16194615]

Kinney HC, Brody BA, Kloman AS, Gilles FH. Sequence of central nervous system myelination in human infancy. II. Patterns of myelination in autopsied infants. J Neuropathol Exp Neurol. 1988; 47:217–234. [PubMed: 3367155]

Larroche, J., editor. Development of the central nervous system. Excerpta Medica; Amsterdam: 1977.

Le Bihan D, Breton E, Lallemand D, Grenier P, Cabanis E, Laval-Jeantet M. MR imaging of intravoxel incoherent motions: application to diffusion and perfusion in neurologic disorders. Radiology. 1986; 161:401–407. [PubMed: 3763909]

Lebel C, Walker L, Leemans A, Phillips L, Beaulieu C. Microstructural maturation of the human brain from childhood to adulthood. Neuroimage. 2008; 40:1044–1055. [PubMed: 18295509]

Li Y, Zhu H, Shen D, Lin W, Gilmore JH, Ibrahim JG. Multiscale adaptive regression models for neuroimaging data. J R Stat Soc Ser B, Stat Methodol. 2011; 73:559–578.

Liang KY, Zeger SL. Longitudinal data analysis using generalized linear models. Biometrika. 1986; 73:13–22.

Löbel U, Sedlacik J, Güllmar D, Kaiser WA, Reichenbach JR, Mentzel HJ. Diffusion tensor imaging: the normal evolution of ADC, RA, FA, and eigenvalues studied in multiple anatomical regions of the brain. Neuroradiology. 2009; 51:253–263. [PubMed: 19132355]

McKinstry RC, Mathur A, Miller JH, Ozcan A, Snyder AZ, Schefft GL, Almli CR, Shiran SI, Conturo TE, Neil JJ. Radial organization of developing preterm human cerebral cortex revealed by non-invasive water diffusion anisotropy MRI. Cereb Cortex. 2002; 12:1237–1243. [PubMed: 12427675]

Mukherjee P, Miller JH, Shimony JS, Conturo TE, Lee BC, Almli CR, McKinstry RC. Normal brain maturation during childhood: developmental trends characterized with diffusion-tensor MR imaging. Radiology. 2001; 221:349–358. [PubMed: 11687675]

Mukherjee P, Miller JH, Shimony JS, Philip JV, Nehra D, Snyder AZ, Conturo TE, Neil JJ, McKinstry RC. Diffusion-tensor MR imaging of gray and white matter development during normal human brain maturation. AJNR Am J Neuroradiol. 2002; 23:1445–1456. [PubMed: 12372731]

Neil JJ, Shiran SI, McKinstry RC, Schefft GL, Snyder AZ, Almli CR, Akbudak E, Aronovitz JA, Miller JP, Lee BC, Conturo TE. Normal brain in human newborns: apparent diffusion coefficient and diffusion anisotropy measured by using diffusion tensor MR imaging. Radiology. 1998; 209:57–66. [PubMed: 9769812]

Paus T, Collins DL, Evans AC, Leonard G, Pike B, Zijdenbos A. Maturation of white matter in the human brain: a review of magnetic resonance studies. Brain Res Bull. 2001; 54:255–266. [PubMed: 11287130]

Prayer D, Barkovich AJ, Kirschner DA, Prayer LM, Roberts TP, Kucharczyk J, Moseley ME. Visualization of nonstructural changes in early white matter development on diffusion-weighted MR images: evidence supporting premyelination anisotropy. AJNR Am J Neuroradiol. 2001; 22:1572–1576. [PubMed: 11559509]

Provenzale JM, Liang L, DeLong D, White LE. Diffusion tensor imaging assessment of brain white matter maturation during the first postnatal year. Am J Roentgenol. 2007; 189:476–486. [PubMed: 17646476]

Schneider JF, Il'yasov KA, Hennig J, Martin E. Fast quantitative diffusion-tensor imaging of cerebral white matter from the neonatal period to adolescence. Neuroradiology. 2004; 46:258–266. [PubMed: 14999435]

Shen D. Image registration by local histogram matching. Pattern Recognit. 2007; 40:1161–1172.

Sherman D, Brophy PJ. Mechanisms of axon ensheathment and myelin growth. Nat Rev Neurosci. 2005; 6:683–690. [PubMed: 16136172]

Smith SM, Johansen-Berg H, Jenkinson M, Rueckert D, Nichols TE, Miller KL, Robson MD, Jones DK, Klein JC, Bartsch AJ, Behrens TE. Acquisition and voxelwise analysis of multi-subject diffusion data with tract-based spatial statistics. Nat Protoc. 2007; 2:499–503. [PubMed: 17406613]

Song SK, Sun SW, Ju WK, Lin SJ, Cross AH, Neufeld AH. Diffusion tensor imaging detects and differentiates axon and myelin degeneration in mouse optic nerve after retinal ischemia. Neuroimage. 2003; 20:1714–1722. [PubMed: 14642481]

Wedeen VJ, Rosene DL, Wang R, Dai G, Mortazavi F, Hagmann P, Kaas JH, Tseng WY. The geometric structure of the brain fiber pathways. Science. 2012; 335:1628–1634. [PubMed: 22461612]

Wiegell MR, Larsson HB, Wedeen VJ. Fiber crossing in human brain depicted with diffusion tensor MR imaging. Radiology. 2000; 217:897–903. [PubMed: 11110960]

Zhai G, Lin W, Wilber KP, Gerig G, Gilmore JH. Comparisons of regional white matter diffusion in healthy neonates and adults performed with a 3.0-T head-only MR imaging unit. Radiology. 2003; 229:673–681. [PubMed: 14657305]

Zhang J, van Zijl PC, Mori S. Image contrast using the secondary and tertiary eigenvectors in diffusion tensor imaging. Magn Reson Med. 2006; 55:439–449. [PubMed: 16402380]

Zhang J, Evans A, Hermoye L, Lee SK, Wakana S, Zhang W, Donohue P, Miller MI, Huang H, Wang X, van Zijl PC, Mori S. Evidence of slow maturation of the superior longitudinal fasciculus in early childhood by diffusion tensor imaging. Neuroimage. 2007; 38:239–247. [PubMed: 17826183]

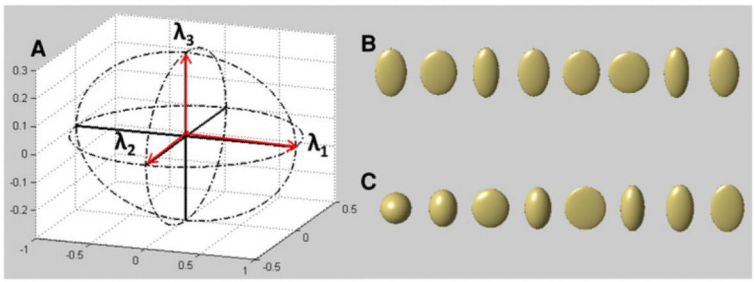

Fig. 1.

Demonstration of the geometrical shape of a diffusion tensor matrix with three eigenvalues representing the water diffusivities ($\lambda_1 = 1$, $\lambda_2 = 0.5$, and $\lambda_3 = 0.3$) along three perpendicular principal directions (*A*). Different shapes of the diffusion tensor matrix can have the same fractional anisotropy (*B*) and mean diffusivity (*C*) as the tensor in (*A*)

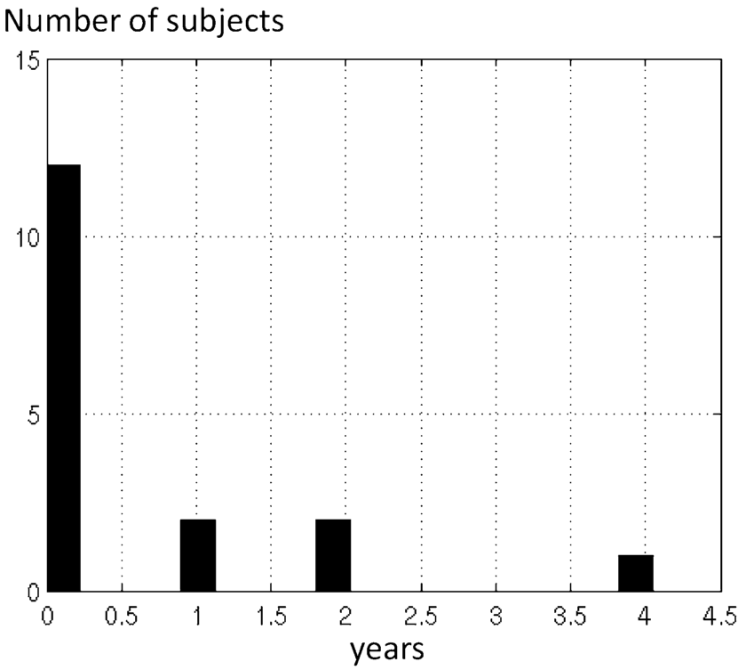

Fig. 2.
The age distribution of the 71 datasets included in this study

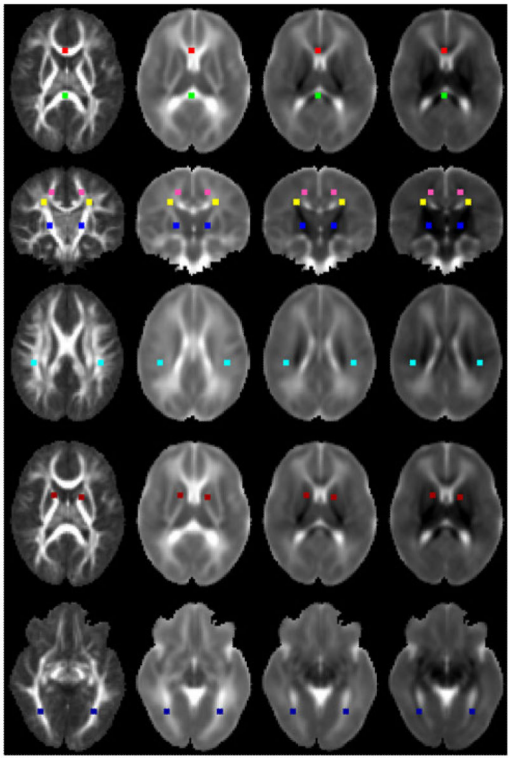

Fig. 3.

The center locations of ROIs in genu (GENU in *red*), splenium (SPLE in *green*), PLIC (*blue*), the fiber crossing area between corona radiata and genu (CROS in *yellow*), anterior corona radiata (CR in *mangneta*), superior longitudinal fasciculus (SLF in *cyan*), anterior limb of internal capsules (ALIC in *dark red*) and inferior longitudinal fasciculus (ILF in *purple*) superimposed on the mean FA (1st column), λ_1 (2nd column), λ_2 (3rd column), and λ_3 (last column) images from the 4-year-olds

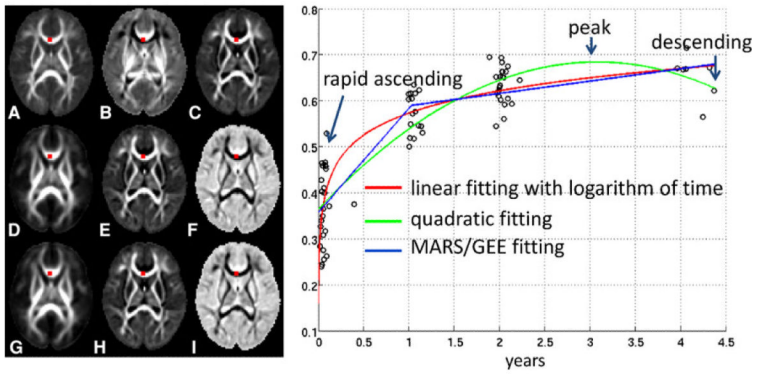

Fig. 4.

The growth trajectories of FA obtained with the three fitting schemes: linear logarithm of time, quadratic, and the proposed MARS/GEE approach. The mean FA images and the intercept and velocity coefficient maps from the linear logarithm of time fitting were given in panels *A–C*, respectively. The intercept, velocity and acceleration coefficient maps from quadratic fitting were given in panels *D–F*, respectively. The coefficient maps for intercept, velocity within **PI** and the velocity transition from **PI** to **PII** obtained with MARS were given in panels *G–I*, respectively. As apparent in panel *B*, the intercept from the linear logarithm fitting generated unrealistically low FA at genu

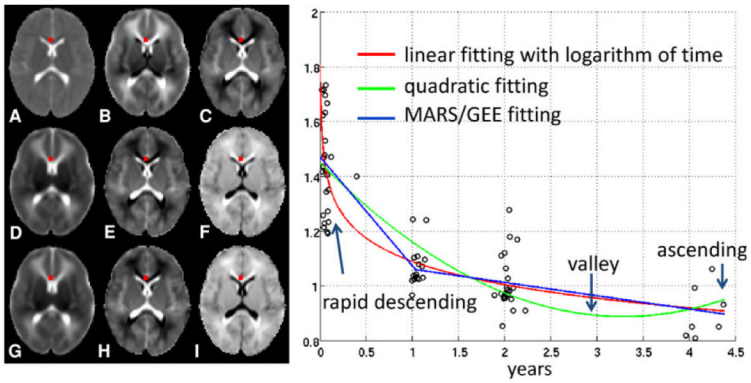

Fig. 5.

The growth trajectories of MD obtained with the three fitting schemes: linear logarithm of time, quadratic, and the proposed MARS/GEE approach. Panels *A–I* represent the same coefficient maps as their counterparts in Fig. 4 but for MD. As shown in panel B, the intercept from the linear logarithm fitting generated unrealistically high MD at genu

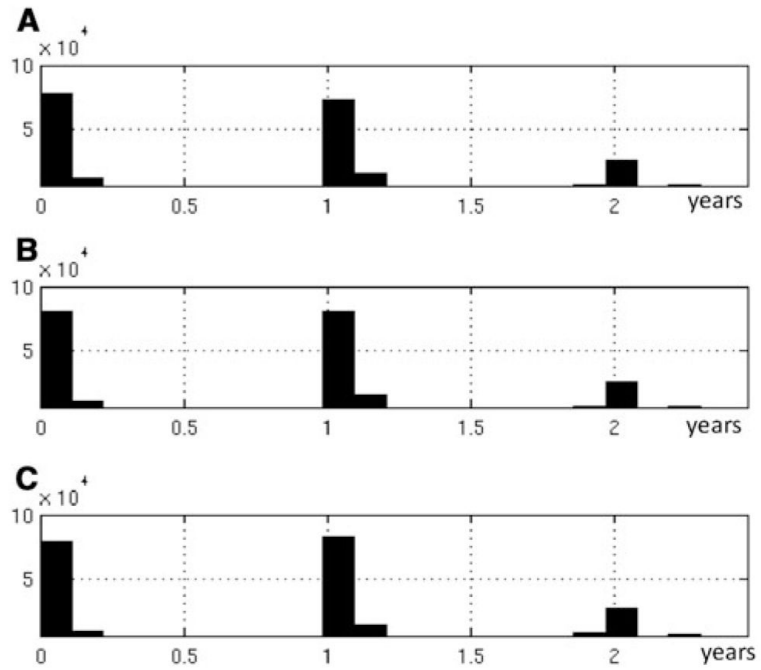

Fig. 6.

Histograms of the knots identified with MARS for λ_1, λ_2 and λ_3 (**a–c**) had almost identical distributions (r = 0.994 between λ_1 and λ_2; r = 0.989 between λ_1 and λ_3; r = 0.998 between λ_2 and λ_3). The three apparent clusters were observed with the medians at 24 days (0.066 years), 377 days (1.033 years), and 739 days (2.025 years) for all three eigenvalues

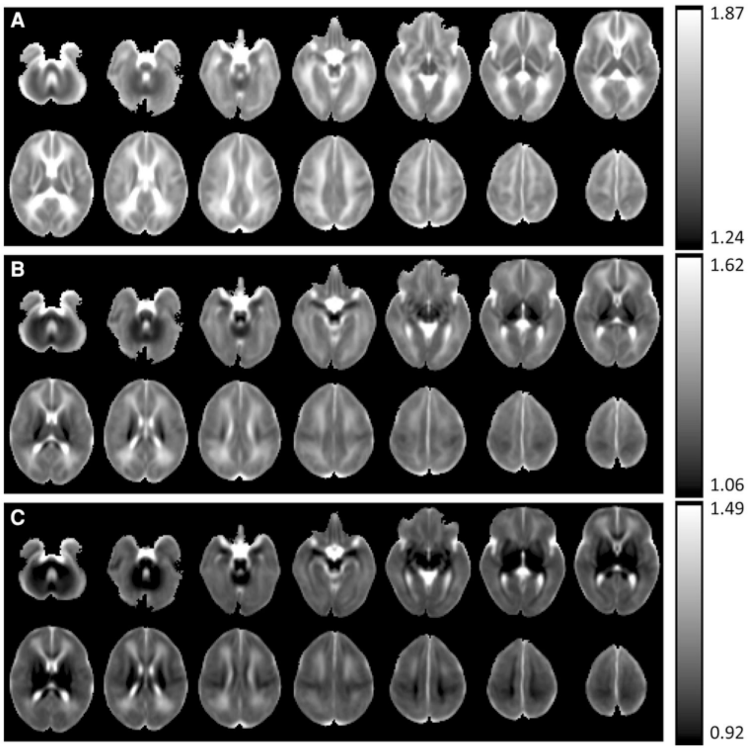

Fig. 7.

The estimated coefficient maps for β_0 (10^{-3} mm^2/s, the intercept term in Eq. 9) with MARS/GEE fitting, which are the estimated maps for the three eigenvalues at birth (**a–c** for λ_1–λ_3). It was apparent that λ_1 had higher values in central than peripheral white matter, while λ_2 and λ_3 assumed a reversed spatial distribution pattern. The minima and maximas used for *color bar* were chosen as 5 and 95 % of the β_0 values from the three eigenvalues, respectively

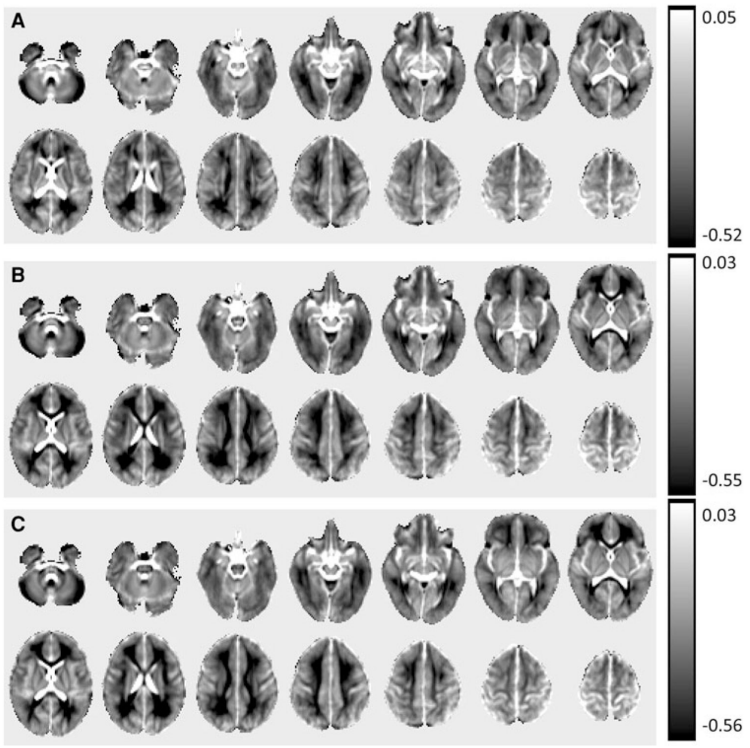

Fig. 8.

The estimated coefficient maps for β_1 (10^{-3} mm^2/(s × year), the velocity in **PI** from Eq. 9) with MARS/GEE fitting for the three eigenvalues (**a–c** for λ_1–λ_3). All three eigenvalues demonstrated reduction in the initial phase. The minima and maxima used for *color bar* were chosen as 5 and 95 % of the β_1 values from the three eigenvalues, respectively

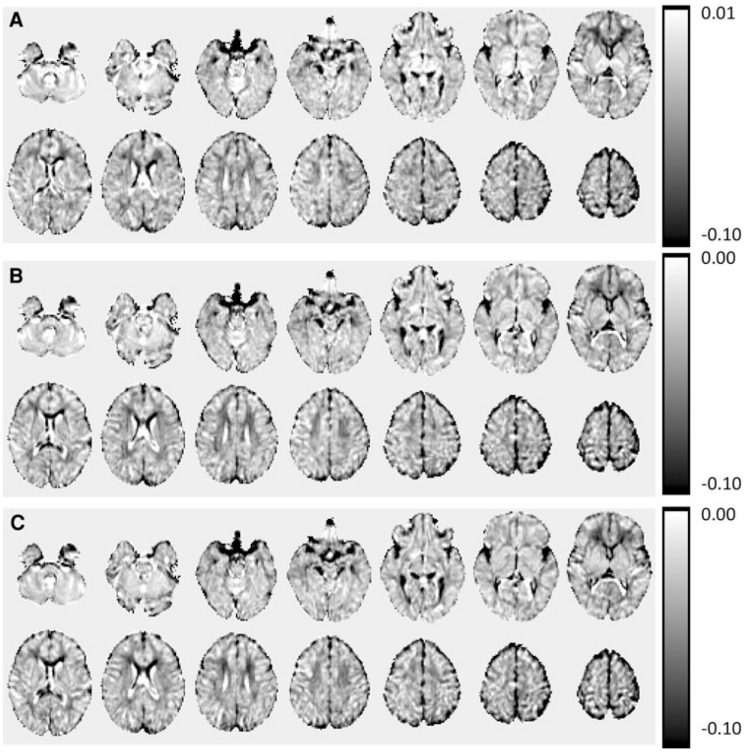

Fig. 9.

The estimated coefficient maps for $\beta_1 + \beta_2$ (the velocity in **PII** from Eq. 9) with MARS/GEE fitting for the three eigenvalues (**a–c** for λ_1–λ_3). All three eigenvalues still remained decreasing during **PII** but with slower magnitudes than during **PI**. The minima and maxima used for *color bar* were chosen as 5 and 95 % of the $\beta_1 + \beta_2$ values from the three eigenvalues, respectively

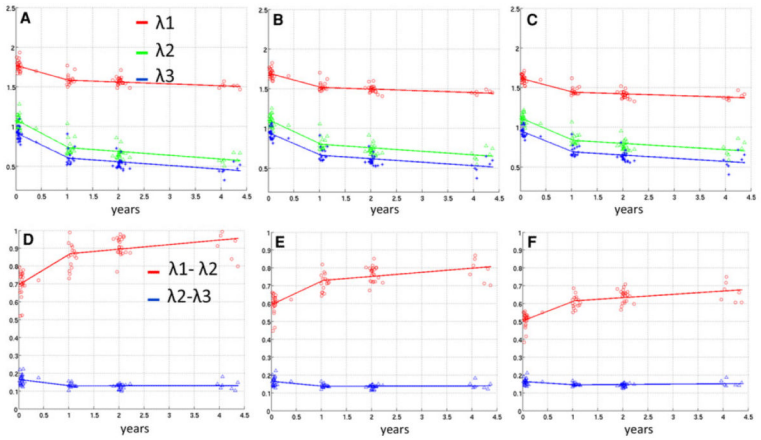

Fig. 10.

The growth trajectories of λ_1, λ_2, and λ3 (**a–c** for ROI1–ROI3) and their differences (**d–f** for ROI1–ROI3) in central white matter obtained with three different sized ROIs

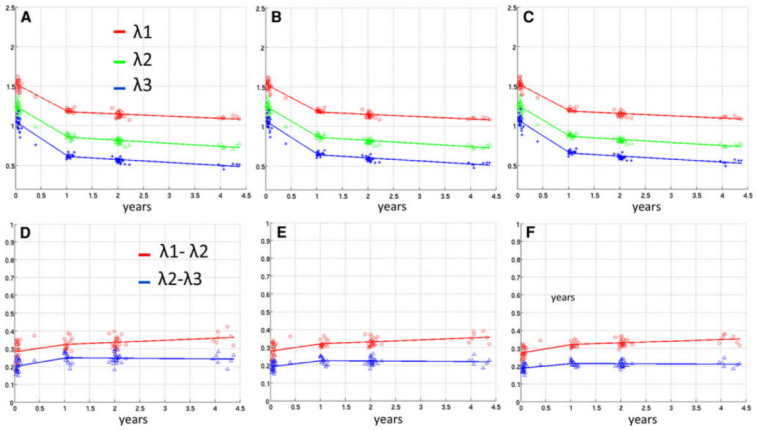

Fig. 11.

The growth trajectories of λ_1, λ_2, and λ3 (**a–c** for ROI1–ROI3) and their differences (**d–f** for ROI1–ROI3) in peripheral white matter obtained with three different sized ROIs

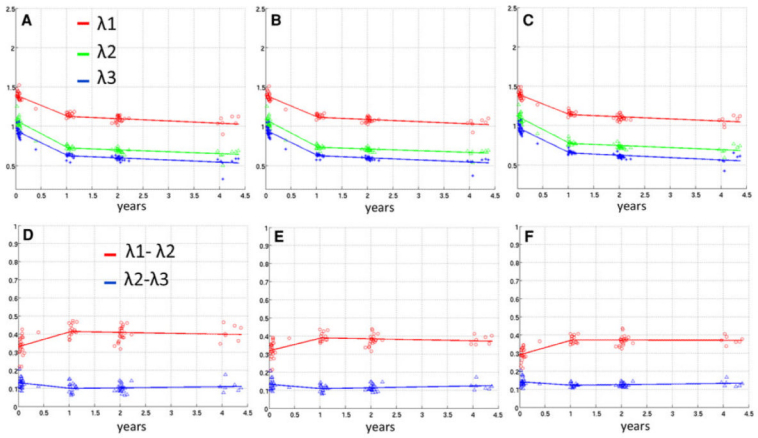

Fig. 12.

The growth trajectories of λ_1, λ_2, and $\lambda 3$ (**a–c** for ROI1–ROI3) and their differences (**d–f** for ROI1–ROI3) in ALIC obtained with three different sized ROIs

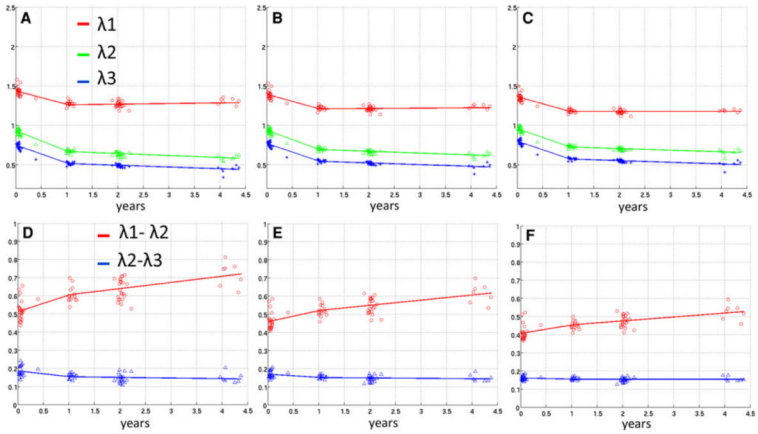

Fig. 13.

The growth trajectories of λ_1, λ_2, and $\lambda 3$ (**a–c** for ROI1–ROI3) and their differences (**d–f** for ROI1–ROI3) in PLIC obtained with three different sized ROIs

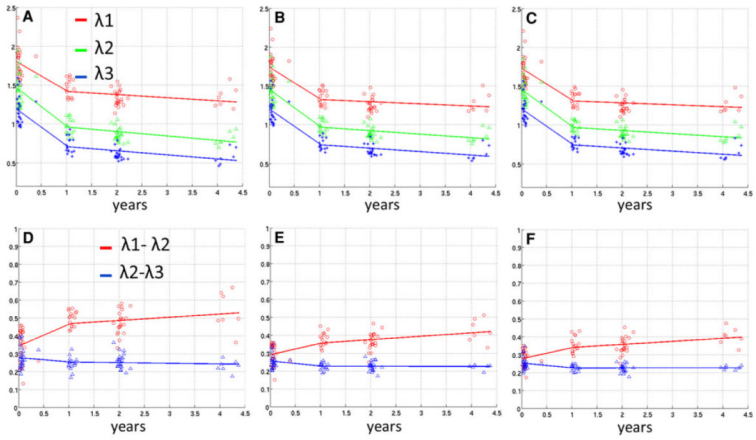

Fig. 14.

The growth trajectories of λ_1, λ_2, and $\lambda 3$ (**a–c** for ROI1–ROI3) and their differences (**d–f** for ROI1–ROI3) in ILF obtained with three different sized ROIs

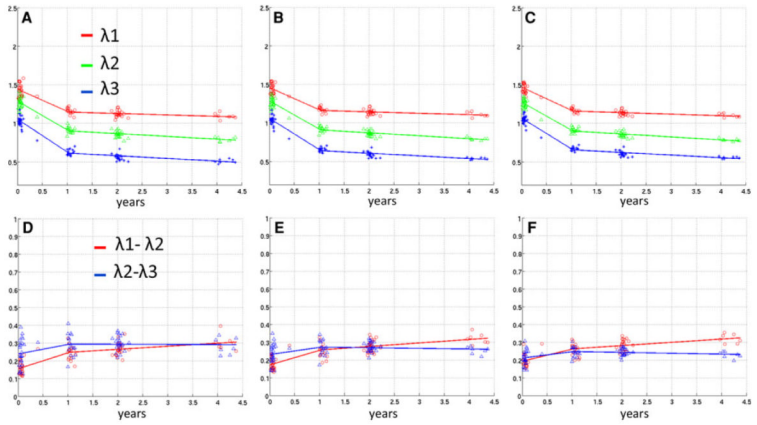

Fig. 15.

The growth trajectories of λ_1, λ_2, and $\lambda 3$ (**a–c** for ROI1–ROI3) and their differences (**d–f** for ROI1–ROI3) in SLF obtained with three different sized ROIs

Table 1

The comparisons of the estimated DTI parameters at birth (β_0), the growth velocities during **PI (V_1)** and **PII (V_2)** for three eigenvalues (λ_1, λ_2, and λ_3), and their differences **D1** (λ_1–λ_2) and **D2** (λ_2–λ_3) within three ROIs of different sizes (ROI1, ROI2, and ROI3) between central and peripheral white matter

	β_0 (central/peripheral)	V_1 (central/peripheral)	V_2 (central/peripheral)
ROI1			
λ_1	1.777 ± 0.358/1.530 ± 0.088$^{\$\$\$}$	−0.181 ± 0.089/−0.343 ± 0.080$^{\$\$\$}$	−0.023 ± 0.038/−0.028 ± 0.011
λ_2	1.081 ± 0.174/1.248 ± 0.061$^{\$\$\$}$	−0.349 ± 0.192/−0.385 ± 0.052*	−0.048 ± 0.042/−0.039 ± 0.009**
λ_3	0.918 ± 0.187/1.049 ± 0.056$^{\$\$\$}$	−0.317 ± 0.187/−0.431 ± 0.066$^{\$\$\$}$	−0.047 ± 0.039/−0.038 ± 0.010**
D1	0.694 ± 0.230/0.281 ± 0.106$^{\$\$\$}$	0.170 ± 0.163/0.041 ± 0.103$^{\$\$\$}$	0.025 ± 0.029/0.012 ± 0.014$^{\$\$\$}$
D2	0.164 ± 0.052/0.199 ± 0.075$^{\$}$	−0.034 ± 0.031/0.047 ± 0.040$^{\$\$\$}$	0.000 ± 0.011/−0.002 ± 0.010
ROI2			
λ_1	1.702 ± 0.358/1.536 ± 0.091$^{\$\$\$}$	−0.175 ± 0.149/−0.343 ± 0.083$^{\$\$\$}$	−0.022 ± 0.037/−0.030 ± 0.014$^{\$\$}$
λ_2	1.107 ± 0.222/1.25 ± 0.074$^{\$\$\$}$	−0.306 ± 0.206/−0.384 ± 0.066$^{\$\$\$}$	−0.045 ± 0.042/−0.040 ± 0.011**
λ_3	0.944 ± 0.217/1.067 ± 0.074$^{\$\$\$}$	−0.282 ± 0.202/−0.416 ± 0.085$^{\$\$\$}$	−0.044 ± 0.039/−0.039 ± 0.011**
D1	0.593 ± 0.226/0.278 ± 0.100$^{\$\$\$}$	0.132 ± 0.164/0.040 ± 0.100$^{\$\$\$}$	0.023 ± 0.031/0.011 ± 0.016$^{\$\$\$}$
D2	0.164 ± 0.050/0.190 ± 0.065$^{\$\$\$}$	−0.026 ± 0.039/0.034 ± 0.049$^{\$\$\$}$	0.000 ± 0.013/−0.002 ± 0.011***
ROI3			
λ_1	1.620 ± 0.345/1.534 ± 0.092$^{\$\$\$}$	−0.171 ± 0.169/0.340 ± 0.082$^{\$\$\$}$	−0.021 ± 0.034/−0.030 ± 0.014$^{\$\$\$}$
λ_2	1.116 ± 0.231/1.262 ± 0.090$^{\$\$\$}$	−0.278 ± 0.192/−0.387 ± 0.076$^{\$\$\$}$	−0.039 ± 0.040/−0.039 ± 0.013
λ_3	0.954 ± 0.221/1.075 ± 0.088$^{\$\$\$}$	−0.263 ± 0.188/−0.412 ± 0.094$^{\$\$\$}$	−0.040 ± 0.038/−0.038 ± 0.012
D1	0.503 ± 0.224/0.273 ± 0.098$^{\$\$\$}$	0.108 ± 0.159/0.047 ± 0.098$^{\$\$\$}$	0.018 ± 0.029/0.009 ± 0.017$^{\$\$\$}$
D2	0.163 ± 0.047/0.186 ± 0.059$^{\$\$\$}$	−0.017 ± 0.044/0.026 ± 0.0526$^{\$\$\$}$	0.002 ± 0.012/−0.001 ± 0.011$^{\$\$\$}$

*(p<0.05,

**p<0.01,

***p<10^{-3},

$^{\$}$$p$<$10^{-4}$,

$^{\$\$}$$p$<$10^{-5}$,

$^{\$\$\$}$$p$<$10^{-6}$)

Table 2

The comparisons between PLIC and ALIC

	β_0 (PLIC/ALIC)	V_1 (PLIC/ALIC)	V_2 (PLIC/ALIC)
ROI1			
λ_1	1.442 ± 0.089/1.402 ± 0.042**	−0.170 ± 0.054/−0.261 ± 0.063$$$	0.008 ± 0.011/−0.029 ± 0.011$$$
λ_2	0.930 ± 0.067/1.072 ± 0.029$$$	−0.260 ± 0.047/−0.342 ± 0.042$$$	−0.026 ± 0.009/−0.025 ± 0.007
λ_3	0.746 ± 0.049/0.941 ± 0.031$$$	−0.229 ± 0.030/−0.312 ± 0.035$$$	−0.022 ± 0.009/−0.028 ± 0.009**
D1	0.512 ± 0.136/0.330 ± 0.068$$$	0.091 ± 0.089/0.082 ± 0.050	0.034 ± 0.013/−0.005 ± 0.012$$$
D2	0.185 ± 0.061/0.131 ± 0.020$$$	−0.031 ± 0.035/−0.030 ± 0.031	−0.003 ± 0.011/0.003 ± 0.004***
ROI2			
λ_1	1.396 ± 0.114/1.397 ± 0.042	−0.180 ± 0.058/−0.270 ± 0.061$$$	0.005 ± 0.012/−0.028 ± 0.011$$$
λ_2	0.938 ± 0.075/1.079 ± 0.035$$$	−0.240 ± 0.046/−0.340 ± 0.039$$$	−0.024 ± 0.010/−0.022 ± 0.008
λ_3	0.768 ± 0.055/0.948 ± 0.038$$$	−0.221 ± 0.035/−0.317 ± 0.038$$$	−0.022 ± 0.009/−0.027 ± 0.009$$$
D1	0.459 ± 0.160/0.318 ± 0.072$$$	0.061 ± 0.086/0.069 ± 0.058	0.028 ± 0.016/−0.006 ± 0.013$$$
D2	0.169 ± 0.052/0.132 ± 0.024$$$	−0.018 ± 0.040/−0.023 ± 0.034	−0.002 ± 0.012/0.005 ± 0.005$$$
ROI3			
λ_1	1.363 ± 0.126/1.403 ± 0.093$$$	−0.180 ± 0.065/−0.254 ± 0.100$$$	0.001 ± 0.014/−0.028 ± 0.015$$$
λ_2	0.957 ± 0.079/1.113 ± 0.101$$$	−0.227 ± 0.046/−0.334 ± 0.062$$$	−0.022 ± 0.012/−0.027 ± 0.020$$
λ_3	0.797 ± 0.065/0.972 ± 0.094$$$	−0.221 ± 0.043/−0.315 ± 0.061$$$	−0.021 ± 0.009/−0.030 ± 0.018$$$
D1	0.406 ± 0.171/0.290 ± 0.084$$$	0.047 ± 0.082/0.080 ± 0.083$$$	0.022 ± 0.017/−0.001 ± 0.018$$$
D2	0.160 ± 0.046/0.141 ± 0.034$$$	−0.006 ± 0.042/−0.019 ± 0.032$$$	−0.000 ± 0.012/0.003 ± 0.010$$

*($p<0.05$,

**$p<0.01$,

***$p<10^{-3}$,

$$p<10^{-4}$,

$$$p<10^{-5}$,

$$$$p<10^{-6}$)

Table 3

The comparisons between ILF and SLF

	β_0 (ILF/SLF)	V_1 (ILF/SLF)	V_2 (ILF/SLF)
ROI1			
λ_1	1.811 ± 0.122/1.443 ± 0.061$^{\$\$\$}$	−0.373 ± 0.138/−0.287 ± 0.041$^{\$\$\$}$	−0.041 ± 0.031/−0.019 ± 0.012$^{\$\$}$
λ_2	1.469 ± 0.093/1.289 ± 0.040$^{\$\$\$}$	−0.497 ± 0.096/−0.377 ± 0.036$^{\$\$\$}$	−0.058 ± 0.039/−0.036 ± 0.011$^{\$}$
λ_3	1.192 ± 0.108/1.050 ± 0.044$^{\$\$\$}$	−0.477 ± 0.105/−0.430 ± 0.068**	−0.053 ± 0.034/−0.035 ± 0.010***
D1	0.343 ± 0.068/0.155 ± 0.035$^{\$\$\$}$	0.121 ± 0.087/0.090 ± 0.040*	0.018 ± 0.030/0.017 ± 0.017
D2	0.278 ± 0.039/0.238 ± 0.067***	−0.024 ± 0.026/0.053 ± 0.051$^{\$\$\$}$	−0.004 ± 0.011/−0.001 ± 0.012
ROI2			
λ_1	1.746 ± 0.138/1.460 ± 0.062$^{\$\$\$}$	−0.406 ± 0.146/−0.288 ± 0.056$^{\$\$\$}$	−0.028 ± 0.025/−0.018 ± 0.013$^{\$\$}$
λ_2	1.456 ± 0.102/1.288 ± 0.051$^{\$\$\$}$	−0.473 ± 0.100/−0.369 ± 0.058$^{\$\$\$}$	−0.046 ± 0.033/−0.038 ± 0.012**
λ_3	1.201 ± 0.108/1.057 ± 0.048$^{\$\$\$}$	−0.448 ± 0.109/−0.409 ± 0.099***	−0.045 ± 0.030/−0.035 ± 0.010$^{\$}$
D1	0.291 ± 0.078/0.172 ± 0.044$^{\$\$\$}$	0.064 ± 0.103/0.082 ± 0.054*	0.019 ± 0.024/0.020 ± 0.018
D2	0.256 ± 0.058/0.230 ± 0.056$	−0.028 ± 0.027/0.041 ± 0.063$^{\$\$}$	−0.001 ± 0.012/−0.004 ± 0.013*
ROI3			
λ_1	1.734 ± 0.143/1.470 ± 0.062$^{\$\$\$}$	−0.409 ± 0.143/−0.300 ± 0.059$^{\$\$\$}$	−0.025 ± 0.025/−0.020 ± 0.013**
λ_2	1.458 ± 0.108/1.277 ± 0.065$^{\$\$\$}$	−0.475 ± 0.100/−0.367 ± 0.063$^{\$\$\$}$	−0.041 ± 0.035/−0.039 ± 0.013
λ_3	1.207 ± 0.113/1.066 ± 0.051$^{\$\$\$}$	−0.451 ± 0.108/−0.402 ± 0.097$^{\$\$}$	−0.040 ± 0.033/−0.034 ± 0.011***
D1	0.277 ± 0.078/0.193 ± 0.064$^{\$\$\$}$	0.062 ± 0.101/0.068 ± 0.068	0.017 ± 0.023/0.018 ± 0.017
D2	0.253 ± 0.060/0.211 ± 0.057$^{\$\$\$}$	−0.026 ± 0.030/0.035 ± 0.062$^{\$\$\$}$	0.000 ± 0.011/−0.005 ± 0.012$^{\$\$\$}$

*($p<0.05$,

** $p<0.01$,

*** $p<10^{-3}$,

$^{\$}$ $p<10^{-4}$,

$^{\$\$}$ $p<10^{-5}$,

$^{\$\$\$}$ $p<10^{-6}$)